Electrical properties of ScN(111) layers grown on semi-insulating GaN(0001) by plasma-assisted molecular beam epitaxy

Duc V. Dinh* and Oliver Brandt

Leibniz-Institut im Forschungsverbund Berlin e.V., Paul-Drude-Institut für Festkörperelektronik, Hausvogteiplatz 5–7, Berlin 10117, Germany

(Received 14 December 2023; revised 12 June 2024; accepted 28 June 2024; published 25 July 2024)

We investigate the electrical properties of nominally undoped, 10–40-nm-thick ScN(111) layers grown on nearly lattice-matched GaN:Fe/Al_2O_3(0001) templates by plasma-assisted molecular beam epitaxy. Hall-effect measurements yield electron concentrations of 0.7–3.1 $\times$ 10^{19} cm^{-3} and mobilities of 50–160 $cm^2\,V^{-1}\,s^{-1}$ at room temperature. The temperature-dependent (4–360 K) conductivity exhibits two distinct regimes, suggesting two-band conduction in an impurity band and the conduction band. Assuming a single shallow donor in ScN and employing the standard two-band conduction model, we extract the carrier density and mobility in these bands. The results reveal nondegenerate characteristics for a 40-nm-thick layer, while thinner layers are weakly degenerate. For the nondegenerate layer, the donor ionization energy amounts to approximately 12 meV. The electron mobility of the layers is limited by ionized-impurity scattering and phonon scattering at low and high temperatures, respectively. Fits with an expression for optical phonon scattering developed for weakly degenerate semiconductors return an effective phonon energy of (61 $\pm$ 5) meV, a value in between the energies of the longitudinal optical ($\approx$ 84 meV) and transverse optical ($\approx$ 45 meV) phonon modes in ScN.

DOI: 10.1103/PhysRevApplied.22.014067

I. INTRODUCTION

ScN is an emerging group-III transition-metal nitride semiconductor crystallizing in the rocksalt structure. The electronic band structure of ScN is characterized by an indirect gap at about 0.9 eV between the X and Γ points [1–5], a direct gap at about 2 eV at the X point [1–4,6–13], and higher direct gaps at the Γ point of about 3.89 [3–5,13], 5.33 [3,13], and 6.95 eV [3,13].

ScN has attracted significant interest in recent years for its diverse properties and applications [14,15] in fields such as thermoelectrics [12,16,17] and infrared optoelectronics [18]. Due to its close lattice match to GaN ($\Delta a/a \approx 0.1\%$) and a large polarization discontinuity at the ScN(111)/GaN{0001} interface, ScN is also considered a very promising material for high-density two-dimensional electron and hole gases [19]. In addition, ScN has attracted much interest in the form of alloys with the conventional group-XIII nitrides, i.e., GaN, AlN, and InN, due to their high piezoelectric coupling coefficients [20,21]. In particular, the ternary alloy (Sc,Al)N holds great potential for applications in piezoelectric energy harvesting [15], bulk- [22,23] and surface-acoustic-wave devices [24,25], field-effect transistors [26–29], and as a novel ferroelectric material [30,31].

Regarding its electrical properties, nominally undoped ScN is invariably n-type with electron densities n_H ranging from 10^{19} to 10^{21} cm^{-3} at room temperature [3,4,6,8,12,13,17,32–34]. In sputter-deposited material, high n_H values often stem from contamination of the target with F [3,16], but O incorporation [4,8,16] and N vacancies (V_N^+) [16] in ScN are also discussed as potential donors. In materials synthesized by hydride vapor-phase epitaxy, high n_H values are attributed to O [10], but H and Cl have also been suggested [6]. In molecular beam epitaxy (MBE), the high n_H values almost certainly originate from O [13,32] present in the Sc ingot [35,36], with V_N^+ remaining a potential source of electrons for Sc-rich growth conditions [7]. The lowest n_H value of 3.7 $\times$ 10^{18} cm^{-3} and simultaneously the highest mobility (μ_H) of 284 $cm^2\,V^{-1}\,s^{-1}$ at room temperature were reported for 40-μm-thick ScN layers grown on Al_2O_3 substrates by hydride vapor-phase epitaxy, and these were attributed to the low impurity concentrations in those layers (in particular, [O] $<$ 1 $\times$ 10^{18} cm^{-3}) [10].

Several groups have investigated the electrical transport in unintentionally doped n-type ScN using temperature-dependent Hall-effect measurements [4,12,32–34]. With the commonly observed background doping levels ranging from 10^{20}–10^{21} cm^{-3}, ScN is highly degenerate; i.e., n_H does not depend on temperature [4,32,34]. In addition, the μ_H values of these layers have been found to be independent of temperature [32] or to only weakly decrease

*Contact author: dinh@pdi-berlin.de

with increasing temperature [4,34]. It has been suggested that the low mobility observed in the former case possibly arises from boundary scattering in the twinned ScN(111) films [32].

The decrease of mobility with increasing temperature has been analyzed quantitatively in only a few studies [6,37]; in these works, the temperature dependence was found to follow a $T^{-\alpha}$ dependence, with α being close to the exponent 3/2 expected for acoustic phonon scattering. Other authors, not attempting a quantitative analysis, have attributed this decrease of mobility to dislocation scattering [12] or optical phonon scattering [4,34]. In fact, theory shows that optical rather than acoustic phonon scattering should be the dominant mechanism [5].

In this article, we investigate the electrical properties of 10–40-nm thick ScN(111) layers grown on nearly lattice-matched Fe-doped GaN(0001) templates using plasma-assisted molecular beam epitaxy (PAMBE). The electrical properties of the layers are investigated in detail by temperature-dependent Hall-effect measurements, yielding comparatively low electron concentrations of 0.7–3.1 $\times$ 10^{19} cm^{-3} and comparatively high mobilities of 50–160 $cm^2\,V^{-1}\,s^{-1}$ at room temperature. At the same time, the data reveal the presence of parallel conduction originating from both impurity and conduction bands. The electron density and mobility in the conduction band are extracted using a standard two-band conduction model and analyzed with models valid for weakly degenerate semiconductors. The temperature dependence of the electron mobility in the conduction band is limited by ionized-impurity scattering at low temperatures and by optical phonon scattering at high temperatures. Peak values up to 280 $cm^2\,V^{-1}\,s^{-1}$ are observed at temperatures of 140–180 K, and these are among the highest mobilities ever reported for ScN.

II. EXPERIMENTAL

ScN layers are grown by PAMBE on semi-insulating Fe-doped GaN (GaN:Fe) layers deposited by metal-organic vapor-phase epitaxy on Al_2O_3(0001) substrates [38]. These templates consist of a 2-μm-thick GaN:Fe layer ([Fe] = 1 $\times$ 10^{18} cm^{-3}) followed by a 250-nm-thick undoped GaN layer to prevent Fe segregating into the ScN layers. Before being loaded into the ultrahigh-vacuum environment, the GaN templates are etched in an HCl solution to remove the surface oxide and surface contaminants, and they are then rinsed with deionized water and finally blown dry with a nitrogen gun. After this, the templates are outgassed for 2 h at 500 °C in a load-lock chamber attached to the MBE system. The MBE growth chamber is equipped with high-temperature effusion cells to provide the group-XIII and -III metals, including 7N-pure Ga and 5N-pure Sc (note that these purity levels refer to trace metals but not to elements such as N, C, or O), respectively. To prevent the crucible from breaking, the Sc source is kept below the melting point of Sc (1541 °C), which means that the Sc ingot remains granular and porous. A Veeco UNI-Bulb radio-frequency plasma source is used for the supply of active nitrogen (N^*). We use 6N-pure N_2 gas as precursor, and this is further purified by a getter filter. The N^* flux is calculated from the thickness of a GaN layer grown under Ga-rich conditions and thus with a growth rate limited by the N^* flux. Prior to ScN growth, a 100-nm-thick undoped GaN buffer layer is grown at 700 °C under Ga-bilayer conditions. Subsequently, ScN layers are grown at the same temperature under N^*-rich conditions with thicknesses (d_{ScN}) ranging from 10 to 40 nm. These values are determined by fitting experimental triple-axis 2θ–ω x-ray diffraction scans with simulated profiles using the freely available software package InteractiveXRDFit [39] (see Fig. S1 of the supplementary material [40]).

The layers exhibit excellent structural and morphological properties, as evidenced in Figs. S1 and S2 of the supplementary material [40]. For surface chemical analysis, x-ray photoelectron spectroscopy (XPS) measurements are performed using a Scienta Omicron™ system equipped with an Al anode (Al Kα: $h\nu$ = 1486 eV) under ultrahigh vacuum conditions. XPS surveys are conducted before and after Ar^+ sputtering with the intention to remove surface oxides and contaminants (see Fig. S3 of the supplementary material [40]). Information regarding impurities in the Sc ingot, as provided by the commercial vendor, is presented in Fig. S4 of the supplementary material [40]. Raman spectra of all the layers are recorded at room temperature using a Horiba LabRAM HR Evolution™ Raman microscope using a 473-nm diode-pumped solid-state laser for excitation (see Fig. S5 of the supplementary material [40]).

To investigate the electrical properties of the ScN layers, we carry out Hall-effect measurements in the van der Pauw configuration at 4–360 K. A magnetic field of 0.7 T is applied for these measurements. For comparison, temperature-dependent Hall-effect measurements are also performed on a ScN/Al_2O_3(0001) reference layer [13]. The room-temperature carrier density (n_H) and mobility (μ_H) of the ScN/GaN layers are summarized in Table I, along with the values for the conduction band (CB) after accounting for parallel impurity-band (IB) conduction. Despite the nominally identical growth conditions, the values are seen to scatter significantly, with some samples displaying higher mobility despite a higher carrier density, indicating a varying degree of compensation. We believe that these variations are the result of an inhomogeneous distribution of trace impurities in the Sc ingot due to its granular and porous nature. Note that the undoped 100-nm-thick GaN buffer layer grown on the semi-insulating GaN:Fe template is fully depleted and thus too resistive to be measured in our Hall setup. The electrical depletion is consistent with the background carrier density of 1 $\times$ 10^{16} cm^{-3} measured for thick GaN layers grown in the same MBE system.

TABLE I. Overview of the electrical properties of our ScN/GaN layers with thickness d_{ScN}, showing the total [n_H (μ_H)] and conduction-band [n_{CB} (μ_{CB})] electron densities (mobilities) at room temperature.

d_{ScN} (nm)	10	15	20	40
n_H (cm^{-3})	3.1×10^{19}	1.6×10^{19}	2.7×10^{19}	0.7×10^{19}
n_{CB} (cm^{-3})	1.8×10^{19}	7.4×10^{18}	1.2×10^{19}	3.4×10^{18}
μ_H (cm^2 V^{-1} s^{-1})	158	48	88	127
μ_{CB} (cm^2 V^{-1} s^{-1})	204	71	130	176

III. RESULTS AND DISCUSSION

A. Two-band conduction

Figure 1 shows the temperature dependence of n_H and μ_H for two ScN(111) layers on Fe-doped GaN(0001) with different thicknesses. Compared with the ScN(111) reference layer on Al_2O_3(0001) (see Fig. S6 of the supplementary material [40]), the values of n_H and μ_H are more than 1 order of magnitude lower and almost 2 orders of magnitude higher, respectively. Furthermore, both n_H and μ_H exhibit a characteristic dependence on temperature, in contrast to the temperature-independent behavior observed for the degenerate reference layer. Note that all samples are unambiguously *n*-type at any temperature. We do not see any evidence for a two-dimensional hole gas at the ScN(111)/GaN(0001) interface as recently predicted on theoretical grounds [19].

The comparatively low electron densities suggest a significantly lower concentration of O in the layers on GaN as compared with those on Al_2O_3. This finding confirms our previous conclusion that the abundance of O in ScN layers on Al_2O_3 is partly due to out-diffusion from the substrate [13]; however, the corresponding reduction in the density of ionized impurities cannot account for the drastically enhanced mobility. Since ScN(111) layers on both GaN(0001) and Al_2O_3(0001) exhibit a high density of twin boundaries, the factor limiting the mobility for the latter substrate is most likely the very high density of misfit dislocations resulting from the lattice mismatch ($\approx$ 16%) for ScN/Al_2O_3. These misfit dislocations are absent for ScN/GaN due to the virtual lattice match ($\approx$ 0.1%).

Both n_H and μ_H display the textbook-like behavior of a nondegenerate semiconductor at high temperatures. Specifically, n_H increases with increasing temperature because of the thermal activation of electrons from shallow donors to the CB [41], and μ_H increases and then decreases with increasing temperature due to the combined effects of ionized-impurity and phonon scattering [42]. Our data, however, deviate from this behavior at lower temperatures. In particular, n_H reaches a minimum at a certain temperature T_{IB} and then increases again, until it saturates at temperatures <30 K. Simultaneously, μ_H saturates at the same temperature. This behavior has been observed in many semiconductors and is indicative of a gradual change from transport in an IB and in the CB at low and high temperatures, respectively [43–54]. Depending on the impurity concentration, the transport in the IB can proceed via hopping with a finite activation energy or exhibit a metallic character.

In the presence of two-band conduction, the total conductivity (σ_H) can be expressed as the sum of the conductivities in the impurity (σ_{IB}) and conduction bands (σ_{CB}), which are commonly assumed to be thermally activated [55]:

$$\sigma_H = \sigma_{CB} + \sigma_{IB} = a_1 e^{-\frac{E_{a1}}{k_B T}} + a_2 e^{-\frac{E_{a2}}{k_B T}}, \quad (1)$$

where a_1 and a_2 are pre-exponential factors, k_B is the Boltzmann constant and E_{a1} and E_{a2} are activation energies.

Figure 2 shows exemplary conductivity data and a fit with Eq. (1) for the 15-nm-thick ScN layer. The first term (E_{a1} = 18 meV) represents the activation of electrons from the IB to the CB, and this should be close to the actual ionization energy of the dominant donor (i.e., O); in contrast, the second term represents the activation within the IB. In the present case, the fit returns E_{a2} = 16 μeV, close to zero and hence indicating metallic-impurity conduction.

Figure 3 shows the Hall data for the 40-nm-thick ScN film. To decompose these data into the contributions of the IB and the CB, we use the standard two-band conduction model established by Hung [44]:

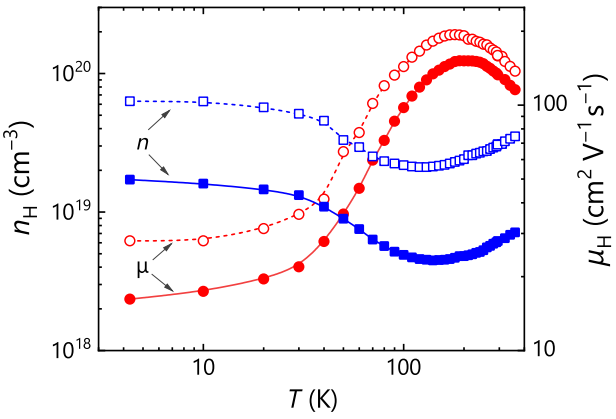

FIG. 1. Temperature dependence of n_H and μ_H for ScN layers with d_{ScN} = 10 nm (□, ○) and d_{ScN} = 40 nm (■, ●).

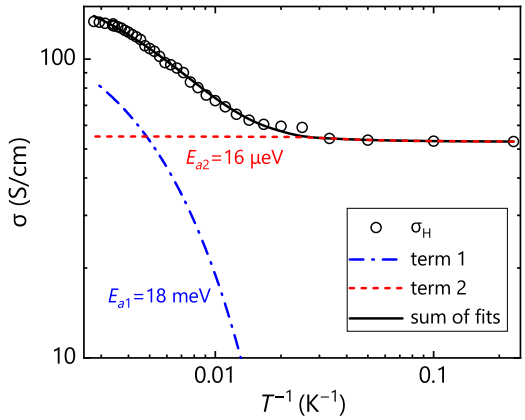

FIG. 2. Double-logarithmic Arrhenius representation of the temperature dependence of σ_H for the 15-nm-thick ScN layer (symbols) and a fit using Eq. (1) (lines).

$$n_H = \frac{(n_{CB}\mu_{CB} + n_{IB}\mu_{IB})^2}{n_{CB}\mu_{CB}^2 + n_{IB}\mu_{IB}^2}, \tag{2a}$$

$$\mu_H = \frac{n_{CB}\mu_{CB}^2 + n_{IB}\mu_{IB}^2}{n_{CB}\mu_{CB} + n_{IB}\mu_{IB}}, \tag{2b}$$

where n_{CB}, μ_{CB}, n_{IB}, and μ_{IB} are the carrier densities and mobilities in the CB and IB, respectively.

Equations (2a) and (2b) contain four unknowns and cannot be solved without additional relations or assumptions. In contrast to two-layer conduction [56,57], for which conduction occurs in parallel but independent channels, the number of carriers in two-band conduction is conserved,

$$n = n_{CB} + n_{IB} = N_d - N_a, \tag{3}$$

eliminating one variable and replacing it with the temperature-independent concentrations of donors (N_d) and acceptors (N_a). In addition, because of the metallic conduction in the IB, we may assume that μ_{IB} is constant and equal to μ_H at 4 K. The remaining two unknown variables are n_{CB} and μ_{CB}. Note that this analysis is based on the presumption of a single shallow donor and a single deep acceptor in ScN. In the case of multiple donor and acceptor species originating, for example, from trace impurities from the Sc source (see Figs. S3–S4 of the supplementary material [40]), obtaining a quantitative understanding of the resulting transport is challenging.

B. Electron density in the conduction band

Values of n_{CB} and μ_{CB} extracted with this procedure are displayed along with the experimental values in Fig. 3 for the case of the 40-nm-thick layer. Analogous values extracted for the other layers are shown in Fig. S7 of the supplementary material [40]. To distinguish between nondegenerate and degenerate layers, this figure also shows the effective conduction-band density of states (N_c), which is given by

$$N_c = \frac{1}{\sqrt{2}}\left(\frac{m^* k_B T}{\pi\hbar^2}\right)^{3/2}, \tag{4}$$

where $m^* = 0.4m_0$ is the density-of-states electron mass of ScN [3,37], and $\hbar$ is the reduced Planck constant. The data displayed in Fig. S7 of the supplementary material [40] show that only the 40-nm-thick layer remains nondegenerate across the whole temperature range, although it approaches degeneracy at temperatures of about 100 K. In contrast, all the other layers are degenerate at all temperatures.

Since even the 40-nm-thick layer is close to degeneracy, we use an expression explicitly derived for weakly degenerate semiconductors by Blakemore [51]. This expression is valid for a Fermi level (E_F) not higher than $1.3k_BT$ above the CB edge (cf. Fig. S8 of the supplementary material [40]):

$$n_{CB} = \frac{2N_c(N_d - N_a)}{\left[N_c + C(N_d - N_a) + \beta^{-1}N_a e^{E_d/k_BT}\right] + \sqrt{\left[N_c - C(N_d - N_a) + \beta^{-1}N_a e^{E_d/k_BT}\right]^2 + 4\beta^{-1}(N_d - N_a)(N_c + CN_a)e^{E_d/k_BT}}}. \tag{5}$$

Here, $C = 0.27$ is a numerical constant that is used to analytically fit the Fermi-Dirac integrals [58], $\beta = 0.5$ is the degeneracy factor [51], and E_d is the donor ionization energy.

Figure 4 shows the n_{CB} values for the 40-nm-thick layer superimposed with a fit to the data using Eqs. (4) and (5) to extract N_d, N_a, and E_d. The best fit is obtained with $N_d = 1 \times 10^{19}$ cm^{-3}, $N_a = 0$, and $E_d = 12$ meV. Fits with finite values for N_a result in negative values for E_d and a larger deviation of the fit from the data.

Despite the fact that the fit is unique and in very satisfactory agreement with the data, the quantitative results are probably inaccurate for two reasons. First, the total

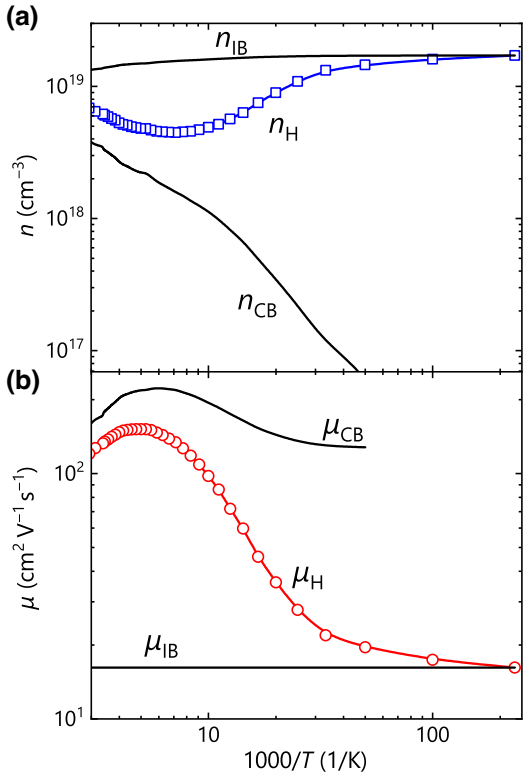

FIG. 3. Double-logarithmic Arrhenius representation of (a) n_H and (b) μ_H for the 40-nm-thick ScN layer. The values of $n_{CB,\,IB}$ in (a) and $\mu_{CB,\,IB}$ in (b) were calculated using Eq. (2).

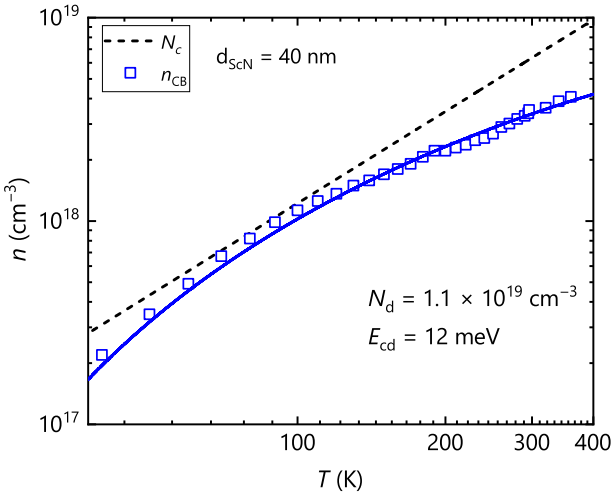

FIG. 4. Fit of n_{CB} for the 40-nm-thick ScN layer using Eqs. (4) and (5). Here, N_c is the effective conduction-band density of states of ScN.

electron density $n = n_H(4\ \mathrm{K}) = 1.7 \times 10^{19}\ \mathrm{cm}^{-3} > N_d - N_a = 1 \times 10^{19}\ \mathrm{cm}^{-3}$, in contradiction of Eq. (3). Second, in view of the limited purity of the Sc source (see Figs. S3–S4 of the supplementary material [40]), we find the complete absence of compensation highly unlikely. Indeed, the 10-nm-thick layer exhibits a higher mobility for simultaneously higher electron density (cf. Table I and Fig. 1), which can only be explained by a considerable degree of compensation for the 40-nm-thick layer. A possible explanation for these discrepancies is the existence of a second, partially filled band formed by deep donors, which is not interacting with the CB but compensating acceptor states. We did not attempt to quantitatively analyze the data with such a three-band model because this would add further unknowns to which we have no experimental access.

The limited thicknesses of the ScN layers under investigation impede secondary-ion mass spectrometry for detecting the most abundant impurities; however, XPS measurements performed on cleaned surfaces indicate that O and C are present in the layers [see Fig. S3(b) of the supplementary material [40]]. While O is well known to preferentially incorporate on N sites and to act as a shallow donor in ScN [3,7,13,37,59], the behavior of C in ScN is less well understood. For GaN [60], density functional theory calculations show that C is amphoteric, with the substitution of C atoms on Ga sites (C_{Ga}) resulting in a shallow donor, while C_N forms deep acceptor states. For ScN, C_N has also been found be a deep acceptor, but the case of C_{Sc} has not been investigated [59]. Extrapolating from GaN, it is likely that C is also amphoteric in ScN. Since the Fermi level is close to the CB, the formation energy of C_N is likely to be lower than that of C_{Sc}. In terms of native point defects, N and Sc vacancies have the lowest formation energies [61]. The former is a singly charged donor (V_N^+) and has been reported to contribute to a high n_H value in ScN grown by PAMBE under Sc-rich conditions [7]. The layers investigated in this study were grown under N*-rich conditions, and the influence of V_N^+ is thus likely to be negligible. The latter is a triply charged acceptor (V_{Sc}^{3-}) and would thus be a highly efficient center compensating shallow donors; however, for non-degenerate ScN, the formation energy of these defects is still very high [61], making it unlikely that they are present in sufficiently high concentrations.

Considering the numerous metal impurities present in the Sc source used to grow the ScN layers in the present work (cf. Fig. S4 of the supplementary material [40]), only a few are present with a concentration that can affect the electrical properties of the layers. With a concentration close to $1 \times 10^{19}\ \mathrm{cm}^{-3}$, Fe is the foremost of these candidates. While Fe is known as a deep acceptor in GaN [62], its behavior in ScN is unknown. Si is dominantly a shallow donor in GaN, but it may be amphoteric in ScN. Finally, Mg has been found to act as a shallow acceptor in ScN [59].

C. Electron mobility and scattering mechanisms

The scattering processes limiting the electron or hole mobilities of many semiconductors have been investigated in great detail. For materials as diverse as Ge [63], GaAs [64], GaN [65], and β-Ga_2O_3 [66], ionized-impurity, acoustic phonon, and optical phonon scattering are found to determine the mobility at low, medium, and high temperatures, respectively. For heteroepitaxial materials such as GaN, dislocation scattering may also play a role [67]; however, for ScN, such an understanding has not been reached because most layers are highly degenerate and thus do not exhibit a clear dependence of mobility on temperature. In the few cases in which a quantitative analysis has been possible, the high-temperature slope has been found to follow a power law with an exponent close to that expected for acoustic phonon scattering [6,37]. Conversely, optical phonon scattering is predicted on theoretical grounds to actually dominate scattering at high temperatures [5].

To investigate this question in more detail, we first consider a phenomenological expression combining acoustic phonon and ionized-impurity scattering [68]:

$$\mu_{\mathrm{CB}} = \left[\left(aT^{-\alpha}\right)^{-1} + \left(bT^{\gamma}\right)^{-1}\right]^{-1}, \tag{6}$$

where the exponents α and γ represent the respective temperatures and a and b are constants. For nondegenerate semiconductors, $\alpha = 1.5$ and $\gamma = 1.5$ are both theoretically expected and experimentally observed [63–66].

Figure 5(a) shows fits of μ_{CB} for the 10- and 40-nm-thick layers obtained using Eq. (6). Evidently, excellent fits are obtained for both samples, returning values of $\alpha = 1.9 \pm 0.2$ and $\gamma = 0.55 \pm 0.2$. The former of these values is close to the value of 1.85 reported by Dismukes *et al.* [6]; the latter is smaller than that expected for ionized-impurity scattering in a nondegenerate material, since the layers are either close to degeneracy at lower temperatures or weakly degenerate, for which the temperature dependence of ionized-impurity scattering flattens [69].

Second, we examine the same data using an expression in which the term representing acoustic phonon scattering is replaced by the characteristic temperature dependence for optical phonon scattering in weakly degenerate semiconductors [68]:

$$\mu_{\mathrm{CB}} = \left[\frac{1}{c}\left(e^{E_{\mathrm{ph}}/k_B T} + 1\right)^{-1} + \left(dT^{\gamma}\right)^{-1}\right]^{-1}, \tag{7}$$

where E_{ph} is the effective phonon energy and c and d are constants. Fits using Eq. (7) are shown in Fig. 5(b), and these are seen to be only marginally different from those displayed in Fig. 5(a). In fact, the goodness of fit as expressed by the adjusted coefficient of determination (adjusted R^2) is essentially identical. The effective phonon energy $E_{\mathrm{ph}} = (61 \pm 5)$ meV returned from the fits falls within the range of phonon energies typically observed for longitudinal optical (≈ 84 meV) and transverse optical (≈ 45 meV) phonon modes in ScN (see the Raman data of the ScN/GaN layers in Fig. S5 of the supplementary material [40]).

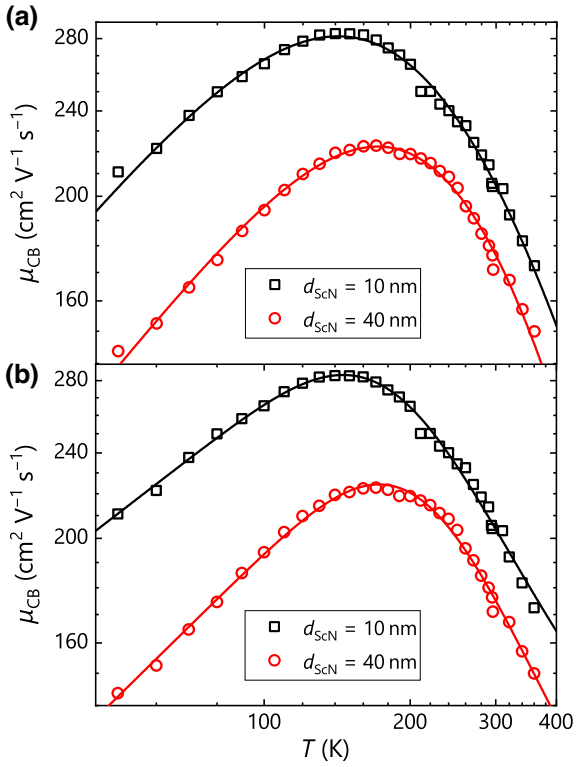

FIG. 5. Fits of μ_{CB} for the 10- and 40-nm-thick ScN layers using (a) Eq. (6) and (b) Eq. (7).

The reason for the inability to clearly distinguish between a power-law and an exponential temperature dependence is the comparatively low contrast between the peak mobility at 140–160 K and the mobility at 360 K, which in turn is a direct consequence of the dominant ionized-impurity scattering. Note that our layers exhibit rather low electron densities and high mobilities compared with most other reports, except for that of Oshima *et al.* [10].

IV. SUMMARY AND CONCLUSIONS

We have presented an in-depth analysis of the electrical properties of ScN(111) layers grown on nearly lattice-matched Fe-doped GaN(0001) templates by plasma-assisted molecular beam epitaxy. Temperature-dependent Hall measurements of these layers, conducted at 4–360 K in the van der Pauw configuration, have revealed the presence of parallel conduction arising from electrons residing in an impurity and the CB. By employing a two-band conduction model and assuming a single shallow

donor in ScN, the electron densities and mobilities of these bands have been extracted. The 40-nm-thick ScN layer remains nondegenerate across the entire temperature range, allowing us to deduce an ionization energy of 12 meV for the shallow donor. A quantitative analysis of the temperature-dependent mobility reveals that scattering by ionized impurities prevails for temperatures up to 140–180 K, while phonon scattering takes over at higher temperatures. Fits assuming acoustic or optical phonon scattering are essentially indistinguishable; the latter are, however, theoretically predicted to dominate. In fact, the effective phonon energy of (61 ± 5) meV returned from the fit assuming optical phonons is just in between the longitudinal optical (≈ 84 meV) and transverse optical (≈ 45 meV) phonon energies in ScN, lending credit to the interpretation supported by theory. Finally, it is worth noting that we did not observe any evidence for a two-dimensional hole gas at the ScN(111)/GaN(0001) interface as recently predicted by modern polarization theory [19]. For incoherent interfaces, misfit dislocations form charged line defects that may lead to electrical compensation and scattering, but the interface between ScN and GaN is coherent. We speculate that a high density of positively charged point defects such as N vacancies form at the interface analogously to the case of O vacancies in perovskite heterostructures [70].

ACKNOWLEDGMENTS

The semi-insulating GaN:Fe/Al_2O_3(0001) templates used in this work are courtesy of Stefano Leone from the Fraunhofer-Institut für Angewandte Festkörperphysik. We thank Carsten Stemmler for expert technical assistance with the MBE system and Hua Lv for a critical reading of the manuscript.

[1] H. A. Al-Brithen, A. R. Smith, and D. Gall, Surface and bulk electronic structure of ScN(001) investigated by scanning tunneling microscopy/spectroscopy and optical absorption spectroscopy, Phys. Rev. B **70**, 045303 (2004).

[2] B. Saha, J. Acharya, T. D. Sands, and U. V. Waghmare, Electronic structure, phonons, and thermal properties of ScN, ZrN, and HfN: a first-principles study, J. Appl. Phys. **107**, 033715 (2010).

[3] R. Deng, B. D. Ozsdolay, P. Y. Zheng, S. V. Khare, and D. Gall, Optical and transport measurement and first-principles determination of the ScN band gap, Phys. Rev. B **91**, 045104 (2015).

[4] J. S. Cetnar, A. N. Reed, S. C. Badescu, S. Vangala, H. A. Smith, and D. C. Look, Electronic transport in degenerate (100) scandium nitride thin films on magnesium oxide substrates, Appl. Phys. Lett. **113**, 192104 (2018).

[5] S. Mu, A. J. E. Rowberg, J. Leveillee, F. Giustino, and C. G. Van de Walle, First-principles study of electron transport in ScN, Phys. Rev. B **104**, 075118 (2021).

[6] J. P. Dismukes, W. M. Yim, and V. S. Ban, Epitaxial growth and properties of semiconducting ScN, J. Cryst. Growth **13-14**, 365 (1972).

[7] A. R. Smith, H. A. Al-Brithen, D. C. Ingram, and D. Gall, Molecular beam epitaxy control of the structural, optical, and electronic properties of ScN(001), J. Appl. Phys. **90**, 1809 (2001).

[8] M. A. Moram, Z. H. Barber, and C. J. Humphreys, The effect of oxygen incorporation in sputtered scandium nitride films, Thin Solid Films **516**, 8569 (2008).

[9] B. Saha, G. Naik, V. P. Drachev, A. Boltasseva, E. E. Marinero, and T. D. Sands, Electronic and optical properties of ScN and (Sc,Mn)N thin films deposited by reactive DC-magnetron sputtering, J. Appl. Phys. **114**, 063519 (2013).

[10] Y. Oshima, E. G. Víllora, and K. Shimamura, Hydride vapor phase epitaxy and characterization of high-quality ScN epilayers, J. Appl. Phys. **115**, 153508 (2014).

[11] L. Lupina, M. H. Zoellner, T. Niermann, B. Dietrich, G. Capellini, S. B. Thapa, M. Haeberlen, M. Lehmann, P. Storck, and T. Schroeder, Zero lattice mismatch and twin-free single crystalline ScN buffer layers for GaN growth on silicon, Appl. Phys. Lett. **107**, 201907 (2015).

[12] D. Rao, B. Biswas, E. Flores, A. Chatterjee, M. Garbrecht, Y. R. Koh, V. Bhatia, A. I. K. Pillai, P. E. Hopkins, M. Martin-Gonzalez, and B. Saha, High mobility and high thermoelectric power factor in epitaxial ScN thin films deposited with plasma-assisted molecular beam epitaxy, Appl. Phys. Lett. **116**, 152103 (2020).

[13] D. V. Dinh, F. Peiris, J. Lähnemann, and O. Brandt, Optical properties of ScN layers grown on Al_2O_3(0001) by plasma-assisted molecular beam epitaxy, Appl. Phys. Lett. **123**, 112102 (2023).

[14] B. Biswas and B. Saha, Development of semiconducting ScN, Phys. Rev. Mater. **3**, 020301 (2019).

[15] P. Eklund, S. Kerdsongpanya, and B. Alling, Transition-metal-nitride-based thin films as novel energy harvesting materials, J. Mater. Chem. C **4**, 3905 (2016).

[16] S. Kerdsongpanya, N. Van Nong, N. Pryds, A. Žukauskaitė, J. Jensen, J. Birch, J. Lu, L. Hultman, G. Wingqvist, and P. Eklund, Anomalously high thermoelectric power factor in epitaxial ScN thin films, Appl. Phys. Lett. **99**, 232113 (2011).

[17] P. V. Burmistrova, J. Maassen, T. Favaloro, B. Saha, S. Salamat, Y. Rui Koh, M. S. Lundstrom, A. Shakouri, and T. D. Sands, Thermoelectric properties of epitaxial ScN films deposited by reactive magnetron sputtering onto MgO(001) substrates, J. Appl. Phys. **113**, 153704 (2013).

[18] K. C. Maurya, D. Rao, S. Acharya, P. Rao, A. I. K. Pillai, S. K. Selvaraja, M. Garbrecht, and B. Saha, Polar semiconducting scandium nitride as an infrared plasmon and phonon–polaritonic material, Nano Lett. **22**, 5182 (2022).

[19] N. L. Adamski, C. E. Dreyer, and C. G. Van de Walle, Giant polarization charge density at lattice-matched GaN/ScN interfaces, Appl. Phys. Lett. **115**, 232103 (2019).

[20] M. Akiyama, T. Kamohara, K. Kano, A. Teshigahara, Y. Takeuchi, and N. Kawahara, Enhancement of piezoelectric response in scandium aluminum nitride alloy thin films prepared by dual reactive cosputtering, Adv. Mater. **21**, 593 (2009).

[21] F. Tasnádi, B. Alling, C. Höglund, G. Wingqvist, J. Birch, L. Hultman, and I. A. Abrikosov, Origin of the anomalous piezoelectric response in wurtzite $Sc_xAl_{1-x}N$ alloys, Phys. Rev. Lett. **104**, 137601 (2010).

[22] M. Moreira, J. Bjurström, I. Katardjev, and V. Yantchev, Aluminum scandium nitride thin-film bulk acoustic resonators for wide band applications, Vacuum **86**, 23 (2011).

[23] R. Matloub, A. Artieda, C. Sandu, E. Milyutin, and P. Muralt, Electromechanical properties of $Al_{0.9}Sc_{0.1}N$ thin films evaluated at 2.5 GHz film bulk acoustic resonators, Appl. Phys. Lett. **99**, 092903 (2011).

[24] K.-y. Hashimoto, S. Sato, A. Teshigahara, T. Nakamura, and K. Kano, High-performance surface acoustic wave resonators in the 1 to 3 GHz range using a ScAlN/6H-SiC structure, IEEE Trans. Ultrason. Ferroelectr. Freq. Control **60**, 637 (2013).

[25] A. Ding, L. Kirste, Y. Lu, R. Driad, N. Kurz, V. Lebedev, T. Christoph, N. M. Feil, R. Lozar, T. Metzger, O. Ambacher, and A. Žukauskaitė, Enhanced electromechanical coupling in SAW resonators based on sputtered nonpolar $Al_{0.77}Sc_{0.23}N$ $(11\bar{2}0)$ thin films, Appl. Phys. Lett. **116**, 101903 (2020).

[26] M. T. Hardy, B. P. Downey, N. Nepal, D. F. Storm, D. S. Katzer, and D. J. Meyer, Epitaxial ScAlN grown by molecular beam epitaxy on GaN and SiC substrates, Appl. Phys. Lett. **110**, 162104 (2017).

[27] J. Ligl, S. Leone, C. Manz, L. Kirste, P. Doering, T. Fuchs, M. Prescher, and O. Ambacher, Metalorganic chemical vapor phase deposition of AlScN/GaN heterostructures, J. Appl. Phys. **127**, 195704 (2020).

[28] P. Wang, D. Wang, B. Wang, S. Mohanty, S. Diez, Y. Wu, Y. Sun, E. Ahmadi, and Z. Mi, N-polar ScAlN and HEMTs grown by molecular beam epitaxy, Appl. Phys. Lett. **119**, 082101 (2021).

[29] D. V. Dinh, J. Lähnemann, L. Geelhaar, and O. Brandt, Lattice parameters of $Sc_xAl_{1-x}N$ layers grown on GaN(0001) by plasma-assisted molecular beam epitaxy, Appl. Phys. Lett. **122**, 152103 (2023).

[30] P. Wang, D. Wang, S. Mondal, and Z. Mi, Ferroelectric N-polar ScAlN/GaN heterostructures grown by molecular beam epitaxy, Appl. Phys. Lett. **121**, 023501 (2022).

[31] D. Wang, P. Wang, S. Mondal, M. Hu, D. Wang, Y. Wu, T. Ma, and Z. Mi, Thickness scaling down to 5 nm of ferroelectric ScAlN on CMOS compatible molybdenum grown by molecular beam epitaxy, Appl. Phys. Lett. **122**, 052101 (2023).

[32] J. Casamento, J. Wright, R. Chaudhuri, H. G. Xing, and D. Jena, Molecular beam epitaxial growth of scandium nitride on hexagonal SiC, GaN, and AlN, Appl. Phys. Lett. **115**, 172101 (2019).

[33] T. Ohgaki, K. Watanabe, Y. Adachi, I. Sakaguchi, S. Hishita, N. Ohashi, and H. Haneda, Electrical properties of scandium nitride epitaxial films grown on (100) magnesium oxide substrates by molecular beam epitaxy, J. Appl. Phys. **114**, 093704 (2013).

[34] H. Al-Atabi, Q. Zheng, J. S. Cetnar, D. Look, D. G. Cahill, and J. H. Edgar, Properties of bulk scandium nitride crystals grown by physical vapor transport, Appl. Phys. Lett. **116**, 132103 (2020).

[35] J. Casamento, H. G. Xing, and D. Jena, Oxygen incorporation in the molecular beam epitaxy growth of $Sc_xGa_{1-x}N$ and $Sc_xAl_{1-x}N$, Phys. Status Solidi (b) **257**, 1900612 (2020).

[36] J. Casamento, H. Lee, C. S. Chang, M. F. Besser, T. Maeda, D. A. Muller, H. G. Xing, and D. Jena, Strong effect of scandium source purity on chemical and electronic properties of epitaxial $Sc_xAl_{1-x}N$ heterostructures, APL Mater. **9**, 091106 (2021).

[37] B. Saha, M. Garbrecht, J. A. Perez-Taborda, M. H. Fawey, Y. R. Koh, A. Shakouri, M. Martin-Gonzalez, L. Hultman, and T. D. Sands, Compensation of native donor doping in ScN: carrier concentration control and p-type ScN, Appl. Phys. Lett. **110**, 252104 (2017).

[38] S. Leone, F. Benkhelifa, L. Kirste, C. Manz, S. Mueller, R. Quay, and T. Stadelmann, Suppression of iron memory effect in GaN epitaxial layers, Phys. Status Solidi B **255**, 1700377 (2018).

[39] C. Lichtensteiger, InteractiveXRDFit: a new tool to simulate and fit x-ray diffractograms of oxide thin films and heterostructures, J. Appl. Crystallogr. **51**, 1745 (2018).

[40] See Supplemental Material at http://link.aps.org/supplemental/10.1103/PhysRevApplied.22.014067 for: (1) high-resolution 2θ–ω x-ray diffraction (XRD) scan and corresponding simulation and surface morphology of the 20-nm-thick ScN/GaN layer; (2) symmetric 2θ–ω XRD and pole figure measurements for the ScN 002 reflection of the 20-nm-thick ScN/GaN layer; (3) XPS spectra of a ScN layer measured before and after Ar^+ sputtering; (4) metallic trace contamination of the Sc source supplied by the commercial vendor; (5) Raman spectrum of the 40-nm-thick layer; (6) temperature-dependent Hall-effect measurements of the 40-nm-thick ScN/GaN layer and a ScN/Al_2O_3 reference layer; (7) n_{CB} and μ_{CB} values of ScN layers with different thicknesses; (8) $(E_F - E_c)/k_BT$ as a function of temperature calculated for the 40-nm-thick layer.

[41] J. S. Blakemore, in *Semiconductor Statistics* (Pergamon, Oxford, England, UK, 1962), p. 75.

[42] K. Seeger, in *Semiconductor Physics*, 4th ed., edited by M. Cardona, P. Fulde, K. von Klitzing, H.-J. Queisser, and H. K. V. Lotsch, Springer series in Solid-State Sciences, Vol. 40 (Springer, Berlin Heidelberg, 1989).

[43] C. S. Hung and J. R. Gliessman, The resistivity and Hall effect of germanium at low temperatures, Phys. Rev. **79**, 726 (1950).

[44] C. S. Hung, Theory of resistivity and Hall effect at very low temperatures, Phys. Rev. **79**, 727 (1950).

[45] C. S. Hung and J. R. Gliessman, Resistivity and Hall effect of germanium at low temperatures, Phys. Rev. **96**, 1226 (1954).

[46] F. J. Morin and J. P. Maita, Electrical properties of silicon containing arsenic and boron, Phys. Rev. **96**, 28 (1954).

[47] H. Fritzsche, Electrical properties of germanium semiconductors at low temperatures, Phys. Rev. **99**, 406 (1955).

[48] E. M. Conwell, Impurity band conduction in germanium and silicon, Phys. Rev. **103**, 51 (1956).

[49] N. Mott and W. Twose, The theory of impurity conduction, Adv. Phys. **10**, 107 (1961).

[50] T. Matsubara and Y. Toyozawa, Theory of impurity band conduction in semiconductors: an approach to random lattice problem, Prog. Theor. Phys. **26**, 739 (1961).

[51] J. S. Blakemore, in *Semiconductor Statistics* (Pergamon, Oxford, England, UK, 1962), p. 117.

[52] B. A. Kulp, K. A. Gale, and R. G. Schulze, Impurity conductivity in single-crystal CdS, Phys. Rev. **140**, A252 (1965).
[53] R. J. Molnar, T. Lei, and T. D. Moustakas, Electron transport mechanism in gallium nitride, Appl. Phys. Lett. **62**, 72 (1993).
[54] Z. Kabilova, C. Kurdak, and R. L. Peterson, Observation of impurity band conduction and variable range hopping in heavily doped (010) β-Ga_2O_3, Semicond. Sci. Technol. **34**, 03LT02 (2019).
[55] H. Fritzsche, Resistivity and Hall coefficient of antimony-doped germanium at low temperatures, J. Phys. Chem. Solids **6**, 69 (1958).
[56] R. L. Petritz, Theory of an experiment for measuring the mobility and density of carriers in the space-charge region of a semiconductor surface, Phys. Rev. **110**, 1254 (1958).
[57] D. C. Look, Two-layer Hall-effect model with arbitrary surface-donor profiles: application to ZnO, J. Appl. Phys. **104**, 063718 (2008).
[58] J. S. Blakemore, in *Semiconductor Statistics* (Pergamon, Oxford, England, UK, 1962), p. 354.
[59] Y. Kumagai, N. Tsunoda, and F. Oba, Point defects and p-type doping in ScN from first principles, Phys. Rev. Appl. **9**, 034019 (2018).
[60] J. L. Lyons, A. Janotti, and C. G. Van de Walle, Carbon impurities and the yellow luminescence in GaN, Appl. Phys. Lett. **97**, 152108 (2010).
[61] Y. Kumagai, N. Tsunoda, and F. Oba, Point defects and p-type doping in ScN from first principles, Phys. Rev. Appl. **9**, 034019 (2018).
[62] J. L. Lyons, D. Wickramaratne, and C. G. Van de Walle, A first-principles understanding of point defects and impurities in GaN, J. Appl. Phys. **129**, 111101 (2021).
[63] P. P. Debye and E. M. Conwell, Electrical properties of n-type germanium, Phys. Rev. **93**, 693 (1954).
[64] K. Fletcher and P. N. Butcher, An exact solution of the linearized Boltzmann equation with applications to the Hall mobility and Hall factor of n-GaAs, J. Phys. C: Solid State Phys. **5**, 212 (1972).
[65] H. M. Ng, D. Doppalapudi, T. D. Moustakas, N. G. Weimann, and L. F. Eastman, The role of dislocation scattering in n-type GaN films, Appl. Phys. Lett. **73**, 821 (1998).
[66] T. Oishi, Y. Koga, K. Harada, and M. Kasu, High-mobility β-$Ga_2O_3(\bar{2}01)$ single crystals grown by edge-defined film-fed growth method and their Schottky barrier diodes with Ni contact, Appl. Phys. Express **8**, 031101 (2015).
[67] D. C. Look and J. R. Sizelove, Dislocation scattering in GaN, Phys. Rev. Lett. **82**, 1237 (1999).
[68] A. Bikowski and K. Ellmer, Analytical model of electron transport in polycrystalline, degenerately doped ZnO films, J. Appl. Phys. **116**, 143704 (2014).
[69] C. A. Niedermeier, S. Rhode, K. Ide, H. Hiramatsu, H. Hosono, T. Kamiya, and M. A. Moram, Electron effective mass and mobility limits in degenerate perovskite stannate $BaSnO_3$, Phys. Rev. B **95**, 161202 (2017).
[70] H. Lee, N. Campbell, J. Lee, T. J. Asel, T. R. Paudel, H. Zhou, J. W. Lee, B. Noesges, J. Seo, B. Park, L. J. Brillson, S. H. Oh, E. Y. Tsymbal, M. S. Rzchowski, and C. B. Eom, Direct observation of a two-dimensional hole gas at oxide interfaces, Nat. Mater. **17**, 231 (2018).